wave emerges from the reference point $\boldsymbol{x}_0$ at the time $t = 0$. Note that the wave goes through the probe element $\boldsymbol{x}_j$ at the time $(x_j - x_0)\sin\alpha_q/c$, which gives the delay law to apply for beam steering. The wave then reaches the image point $\boldsymbol{r} = \begin{bmatrix} x & z \end{bmatrix}^T$ at the time $t_q = r_q/c$, with

$$r_q = (x - x_0)\sin\alpha_q + (z - z_0)\cos\alpha_q. \tag{2.31}$$

If there is a point source located at $\boldsymbol{r}$, the scattered wave reaches the receiver $\boldsymbol{x}_j$ a time r'_j/c later. Denoting $g_{qj}(t)$ the timetrace corresponding to the q-plane wave and received by the j-th element, the echo of the scatterer located at $\boldsymbol{r}$ corresponds to the value $G_{qj}((r_q + r'_j)/c)$. PWI forms an image by summing these echoes over the Q transmitted plane waves and all receivers [Mon09; Le 16]:

$$I^{\mathrm{PWI}}(\boldsymbol{r}) := \left| \sum_{q=1}^{Q} \sum_{j=1}^{N} a_{qj}(\boldsymbol{r}) \tilde{G}_{qj}\left(t = \frac{(x - x_0)\sin\alpha_q + (z - z_0)\cos\alpha_q + r'_j}{c}\right) \right| \tag{2.32}$$

The coefficients $a_{qj}(\boldsymbol{r})$ are as in eq. (2.22) optional spatial filters.

Typically, the number of transmitted plane waves is smaller than the number of elements, so the PWI acquisition takes less time than a full matrix capture, and a higher framerate is achievable. As for TFM, a frequency-domain implementation based on Stolt mapping is known [Gar13]. The side lobes of a PWI image may be reduced using a phase coherence factor [Cru17]. The PWI acquisition matrix may be derived from the FMC matrix by summing the delayed signals, which is useful to compare imaging results from the same dataset:

$$G_{qj}(t) = \sum_{i=0}^{N} F_{ij}(t - (x_i - x_0)\sin\alpha_q/c). \tag{2.33}$$

2.7 Multi-view imaging

Multi-view imaging, also known as multi-modal imaging, extends synthetic aperture algorithms to include waves which arise from mode conversions and internal reflections. Consider the inspection configuration shown in fig. 2.4a, which approximates the inspection of the fusion face of a weld, a common scenario in ultrasonic testing. The ultrasonic array is held at a distance from and inclined relative to the top surface of the specimen to ensure good generation of longitudinal and transverse waves. The region of interest, where defects may occur, is not directly below the array. Both the inspected object and the array are immersed in water.

Because of mode conversions and internal reflections in the sample, multiple ultrasonic ray paths connect a probe element to a target point in the sample. Figure 2.4 shows six paths considered in this thesis, with zero or one internal reflection against the back wall and with longitudinal (L) and transverse (T) waves: L, T, LL, LT, TL, TT. For conciseness, the L mode in water is not included in the description of the path as this is the only mode supported in water. In the transmission nomenclature (transmitter to image point), the modes are read from the probe to the image point. In the reception nomenclature (image point to receiver), the modes are read from the image point to the probe. The full ray paths, transmitter–image point–receiver, are obtained by the combination of a transmit path and a receive path from these six. Figure 2.5 illustrates three possible combinations of paths: T–T, LT–T (or T–TL), and LL–TL (or LT–LL).

Multi-view imaging has been successfully applied to SAFT [Doc86; Lor93], TFM [Zha10b], PWI [Le 16], and MUSIC [For12]. Frequency-domain approaches were also developed [Mer20; Skj11]. Similarly to standard phased array testing [AST13], half-skip paths are used in addition to direct paths in flaw sizing. In multi-view TFM, only the ends of vertical cracks and notches are visible in direct views (tip diffraction), whereas their full length are visible in half-skip and views (specular reflection), with usually a higher signal-to-noise ratio, which leads to an accurate flaw sizing [Fel14; Fid12; Sy18b]. Various investigations have demonstrated the suitability and the overall good performance of multi-view TFM for the inspection of notches, cracks, side-drilled holes and welds [Zha10b; Fid10; Lon12; Zha12; Fel14; Fid12; Cha15; Zha17].

A multi-view TFM view is characterised by the times of flight in transmission and in reception. In transmission, the time of flight of the ray between the i-th probe element and the image point $\boldsymbol{r}$ is denoted $\mathcal{T}_i(\boldsymbol{r})$. In reception, the time of flight of the ray between the image point $\boldsymbol{r}$ and the j-th probe element is denoted $\mathcal{T}'_j(\boldsymbol{r})$. The TFM image for the rays characterised by $(\mathcal{T}, \mathcal{T}')$ is defined by (cf. eq. (2.22))

$$I^{\mathcal{T},\mathcal{T}'}(\boldsymbol{r}) := \left| \sum_{i=1}^{N} \sum_{j=1}^{N} a_{ij}(\boldsymbol{r}) \tilde{F}_{ij} \left(t = \mathcal{T}_i(\boldsymbol{r}) + \mathcal{T}'_j(\boldsymbol{r}) \right) \right|. \tag{2.34}$$

The rationale for this algorithm is the same as explained in section 2.5, except that different ray paths are used. Recalling from section 2.2 that the FMC matrix is symmetric, i.e. $F_{ij} = F_{ji}$,

and if furthermore the apodisation coefficients are chosen to satisfy $a_{ij} = a_{ji}$, then

$$I^{\mathcal{T},\mathcal{T}'}(\boldsymbol{r}) = \left| \sum_{i=1}^{N} \sum_{j=1}^{N} a_{ji}(\boldsymbol{r}) \tilde{F}_{ji} \left(\mathcal{T}_i(\boldsymbol{r}) + \mathcal{T}'_j(\boldsymbol{r}) \right) \right| \tag{2.35}$$

$$= \left| \sum_{i=1}^{N} \sum_{j=1}^{N} a_{ij}(\boldsymbol{r}) \tilde{F}_{ij} \left(\mathcal{T}'_i(\boldsymbol{r}) + \mathcal{T}_j(\boldsymbol{r}) \right) \right| \tag{2.36}$$

$$= I^{\mathcal{T}',\mathcal{T}}(\boldsymbol{r}). \tag{2.37}$$

The second transition is obtained by reindexing the double summation. This demonstrates the TFM images $I^{(\mathcal{T}',\mathcal{T})}$ and $I^{\mathcal{T},\mathcal{T}'}$ are identical. As an example from fig. 2.5, the views LT–T and T–TL are identical, and so are LL–TL and LT–LL. From the $p = 6$ paths shown in fig. 2.4, $p^2 = 36$ views are possible, but the number of distinct views, p', reduces to the number of multisets of length 2 from a set of $p = 6$ elements [Wei]

$$p' = \frac{(p+1)!}{2 \times (p-1)!} = \frac{7!}{2 \times 5!} = 21. \tag{2.38}$$

This thesis aims to exploit the richness of information provided by multi-view imaging to improve the characterisation of small defects. A first step is modelling multi-view TFM images, which is the object of the next chapter.

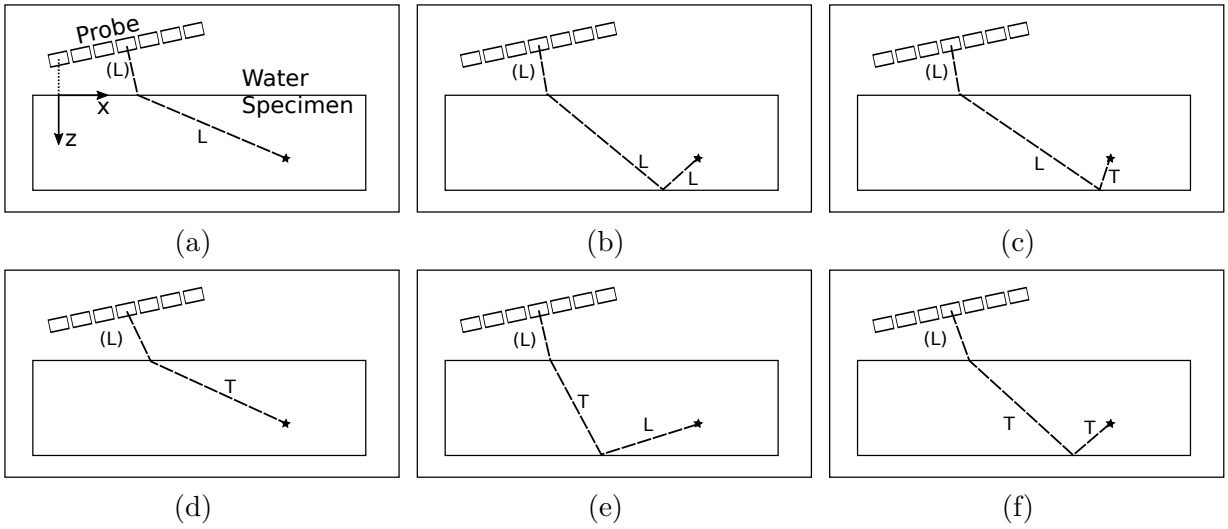

Figure 2.4 – The ray paths considered between an array element and an image point described using transmission nomenclature: (a) L, (b) LL, (c) LT, (d) T, (e) TL, (f) TT. In reception nomenclature, the modes are read from the image point instead of from the array. In both cases, the L mode in water is omitted from the path nomenclature for brevity.

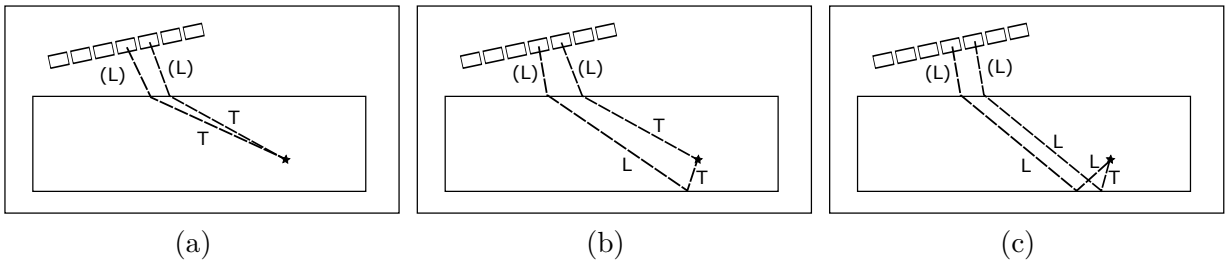

Figure 2.5 – Ray paths in direct, half-skip and full-skip views. (a) View T–T, (b) view LT–T or T–TL, (c) LL–TL or LT–LL.